



Universiteit  
Leiden  
The Netherlands

## **TPHO: a time-dependent photoionization model for AGN outflows**

Rogantini, D.; Mehdipour, M.; Kaastra, J.S.; Costantini, E.; Juráňová, A.; Kara, E.

### **Citation**

Rogantini, D., Mehdipour, M., Kaastra, J. S., Costantini, E., Juráňová, A., & Kara, E. (2022). TPHO: a time-dependent photoionization model for AGN outflows. *The Astrophysical Journal*, 940(2). doi:10.3847/1538-4357/ac9c01

Version: Publisher's Version  
License: [Creative Commons CC BY 4.0 license](https://creativecommons.org/licenses/by/4.0/)  
Downloaded from: <https://hdl.handle.net/1887/3515500>

**Note:** To cite this publication please use the final published version (if applicable).



# TPHO: A Time-dependent Photoionization Model for AGN Outflows\*

Daniele Rogantini<sup>1,2</sup> , Missagh Mehdipour<sup>3</sup> , Jelle Kaastra<sup>2,4</sup>, Elisa Costantini<sup>2,5</sup> , Anna Juráňová<sup>2,5</sup> , and Erin Kara<sup>1</sup> <sup>1</sup>MIT Kavli Institute for Astrophysics and Space Research, Massachusetts Institute of Technology, Cambridge, MA 02139, USA<sup>2</sup>SRON Netherlands Institute for Space Research, Niels Bohrweg 4, 2333 CA Leiden, The Netherlands<sup>3</sup>Space Telescope Science Institute, 3700 San Martin Drive, Baltimore, MD 21218, USA<sup>4</sup>Leiden Observatory, Leiden University, PO Box 9513, 2300 RA Leiden, The Netherlands<sup>5</sup>Anton Pannekoek Astronomical Institute, University of Amsterdam, P.O. Box 94249, 1090 GE Amsterdam, The Netherlands

Received 2022 July 11; revised 2022 October 6; accepted 2022 October 7; published 2022 November 29

## Abstract

Outflows in active galactic nuclei (AGN) are considered a promising candidate for driving AGN feedback at large scales. However, without information on the density of these outflows we cannot determine how much kinetic power they are imparting to the surrounding medium. Monitoring the response of the ionization state of the absorbing outflows to changes in the ionizing continuum provides the recombination timescale of the outflow, which is a function of the electron density. We have developed a new self-consistent time-dependent photoionization model,  $t_{\text{pho}}$ , enabling the measurement of the plasma density through time-resolved X-ray spectroscopy. The algorithm solves the full time-dependent energy and ionization balance equations in a self-consistent fashion for all the ionic species. The model can therefore reproduce the time-dependent absorption spectrum of ionized outflows responding to changes in the ionizing radiation of the AGN. We find that when the ionized gas is in a nonequilibrium state its transmitted spectra are not accurately reproduced by standard photoionization models. Our simulations with the current X-ray grating observations show that the spectral features identified as multicomponent warm absorbers, might in fact be features of a time-changing warm absorber and not distinctive components. The  $t_{\text{pho}}$  model facilitates accurate photoionization modeling in the presence of a variable ionizing source, thus providing constraints on the density and in turn the location of the AGN outflows. Ascertaining these two parameters will provide important insight into the role and impact of ionized outflows in AGN feedback.

*Unified Astronomy Thesaurus concepts:* Photoionization (2060); X-ray active galactic nuclei (2035); Plasma astrophysics (1261)

## 1. Introduction

Accreting supermassive black holes (with mass between  $10^6$  and  $10^9 M_{\odot}$ ) are the central engines of active galactic nuclei (AGN). About half of Seyfert I galaxies show outflows of material in form of ultrafast outflows, warm absorbers, and ionized/neutral/molecular outflows (e.g., Costantini et al. 2007; Fabian 2012; Tombesi et al. 2013, 2015; Veilleux et al. 2013; Kaastra et al. 2014; Fiore et al. 2017; Laha et al. 2021). In the last decades, the potential importance of AGN outflows for the growth of supermassive black holes, the enrichment of the intergalactic medium, the evolution of the host galaxy, cluster cooling flows, and the luminosity function of AGN has been widely recognized (Fabian 2012; Gaspari et al. 2020).

X-ray spectroscopy is a powerful tool to study ionized outflows closer to the central region. Measurement of absorption line spectra yield reliable information on different aspects of the outflows such as their kinematics (turbulence and outflow velocity) and ionization state. Spectral studies of warm absorbers highlight their complex multiphase structure, which spans a wide range of ionization parameters,  $\log(\xi/\text{erg cm s}^{-1}) = -1-3$ , and column densities,  $N_{\text{H}} = 10^{21-23} \text{ cm}^{-2}$  (Blustin et al. 2005;

McKernan et al. 2007; Krongold et al. 2009; Tombesi et al. 2013; Laha et al. 2014; Behar et al. 2017). They are usually detected as absorption lines and edges from H-like and He-like ions of the most abundant elements, such as C, O, N, Ne, Mg, Si, S, and Fe, in the soft spectra below 2 keV (Crenshaw et al. 2003; Mehdipour et al. 2010, 2018; Ebrero et al. 2021). Low-ionization absorbers ( $\log \xi = 0 - 1.5$ ) imprint deep spectral absorption troughs in the rest-frame wavelength 15–17 Å due to the blended Fe M shell unresolved transitions array (UTA; Behar et al. 2001). All these spectral features are always found blueshifted with respect to the systematic redshift, implying that these absorbers are outflowing with a velocity,  $v_{\text{out}}$ , between  $\sim 100$  and  $\sim 5000 \text{ km s}^{-1}$  (Laha et al. 2021).

Spectroscopy on its own does not provide information regarding the distance  $r$  of the absorber material to the central ionizing source. This can be seen within the definition of the ionization parameter  $\xi = L_{\text{ion}}/(n_e r^2)$  where  $L_{\text{ion}}$  is the ionizing luminosity of the source facing the cloud (integrated between 1 and 1000 Ryd) and  $n_e$  is the electron density of the gas (Tarter et al. 1969; Krolik et al. 1981). With  $L_{\text{ion}}$  and  $\xi$  known from observations, only the product  $n_e r^2$  can be determined. This degeneracy makes it challenging to assess the significance of ionized outflows in AGN feedback. The energetics of a spherical shell-like outflow can be quantified by the mass outflow rate,  $\dot{M}_{\text{out}} \simeq 1.23 m_p N_{\text{H}} r v_{\text{out}} \Omega$  and kinetic luminosity,  $\dot{E}_{\text{k}} = \frac{1}{2} \dot{M}_{\text{out}} v_{\text{out}}^2$ , where the constant 1.23 takes into account the abundances of elements,  $m_p$  is the proton mass, and  $\Omega$  is the solid angle subtended by the outflow, which is expected to be  $\sim \pi$  (Blustin et al. 2005). Determining these two quantities

\* Released on ...

Original content from this work may be used under the terms of the [Creative Commons Attribution 4.0 licence](https://creativecommons.org/licenses/by/4.0/). Any further distribution of this work must maintain attribution to the author(s) and the title of the work, journal citation and DOI.

requires precise measurements of the outflow distance to the central source.

A common approach to characterizing the outflow location is measuring the density  $n_e$  of the plasma and deriving the distance through the definition of the ionization parameter. One way to constrain the density via spectroscopy is to use density-sensitive absorption lines from metastable levels (Kraemer et al. 2006; Arav et al. 2015). This method is widely used in UV spectroscopy, where these metastable transitions of C II\*, C III\*, S III\*, and Fe II\* are commonly detected. In the X-ray band, the density diagnostic of AGN outflows using absorption lines is not very effective. The low signal-to noise ratio of these rather weak X-ray lines makes their density diagnostic inaccessible in most AGN (Kaastra et al. 2004; King et al. 2012; Mao et al. 2017). Only the enhanced sensitivity of future X-ray telescopes, such as Arcus (Smith et al. 2016) and Athena (Nandra et al. 2013), and their broader wavelength range will enable the detection of the density-sensitive lines in the X-ray band opening the opportunity for a new kind of diagnostic in AGN outflows (Kaastra 2017).

An alternative method to estimate the gas density is a spectral analysis of density-sensitive emission lines. The ratio between the recombination, intercombination, and forbidden emission lines in the He-like triplets varies as a function of the plasma density (Porquet et al. 2010). In the literature, there are several studies of the He-like triplets in emission from photoionized plasma in AGN where the upper limits of the density are derived (Porquet & Dubau 2000; Collinge et al. 2001; McKernan et al. 2003). However, these spectral analyses are not only limited by the instrumental sensitivity, but also by Li-like absorption lines, which can significantly diminish the intensity of the intercombination line in a photoionized medium, leading to more uncertain density diagnostic (Mehdipour et al. 2015).

The approach that we adopt in this work to determine the gas density is a timing analysis of the response timescale of the plasma to changes in the ionizing radiation. How fast the gas responds depends on the recombination timescale, which is a function of the gas density (see Section 2 for a detailed description). Early time-dependent photoionization studies used only a few spectral features (the most significant) to measure the delay (or the lack of delay) of the ionization state of the gas relative to the ionizing luminosity variation. This constrains the recombination timescale and consequently the density and the distance.

The first attempts at tracing the gas variability with low-resolution CCD instruments, such as BeppoSAX and ASCA, were done studying the evolution of the X-ray absorption edges (Morales et al. 2000). However, the higher energy resolution of the grating on board XMM-Newton (den Herder et al. 2001) and Chandra (Canizares et al. 2005) allowed for meaningfully following the variation of strong absorption lines. For example, Behar et al. (2003) tracked the response of the multiphase warm absorber in RGS data of NGC 3783 investigating the evolution of O VII and O VIII lines for the high-ionization component and the Fe UTA for the low-ionization component. For the same source, Reeves et al. 2004 analyze the variability of the Fe XXV line due to the presence of a possible higher ionization component.

Subsequently, broadband time-dependent photoionization models have been applied to large XMM-Newton and Chandra campaigns such as Mrk 509 (Kaastra et al. 2012), NGC 5548 (Ebrero et al. 2016), and NGC 7469 (Behar et al. 2017;

Mehdipour et al. 2018; Peretz et al. 2018). The complex multicomponent outflow in NGC 4051 is one of the best-studied cases among Seyfert I galaxies (Silva et al. 2016). NGC 4051 is a particularly bright and variable Seyfert I galaxy. Nicastro et al. (1999) and Krongold et al. (2007) suggested a quick response of the absorber ionization to the continuum level that places the absorber as close as 0.003 pc. Recently, Wang et al. (2022) studied the response of an ionized obscurer in NGC 3227, suggesting a location of  $0.001 \text{ pc} \lesssim r \lesssim 0.1 \text{ pc}$  from the central source, whereas the warm absorbers are further out ( $0.01 \text{ pc} \lesssim r \lesssim 100 \text{ pc}$ ).

Here, we present a new time-dependent photoionization model, `tpho`, based on the methodology followed by Kaastra et al. (2012) and Silva et al. (2016). We have upgraded the photoionization code `pion` (Mehdipour et al. 2016) to treat non-photoionization equilibrium state conditions. The ultimate goal of the model is to derive the density and therefore the location of the AGN outflows through precise high-resolution X-ray spectral-timing analysis. In Section 2, we describe the time-dependent effects that have been integrated into the new photoionization model. In Section 3, we show three different applications of the model to describe the impact of time-dependent effects on the inferred plasma physical properties such as temperature, ionic concentration, heating, and cooling rates, etc. The importance of the time-dependent effects in high-resolution X-ray spectroscopy studies of AGN outflows is discussed in Section 4.

## 2. Time-evolving Ionization State

Traditionally, modeling of astronomical photoionized plasma is done assuming the condition of steady-state equilibrium, which means that the gas ionization is balanced by recombination, atomic excitations are balanced by spontaneous and induced de-excitations, and electron heating is balanced by cooling. In this equilibrium condition, it is possible to calculate the distribution of the ionic species in a cloud of optically thin gas illuminated by an intense ionizing luminosity by setting the photoionization rate equal to the radiative recombination rate (see Netzer 1990) and adding the condition for charge conservation (Blandford et al. 1990).

The steady equilibrium assumption is valid only if  $L_{\text{ion}}$  is not varying in time or if the equilibrium timescales for recombination, photoionization, and thermal balance are much shorter than variability timescales in the ionizing continuum. Whenever the illuminating radiation changes on timescales shorter than the equilibrium timescales, it is necessary to take into account the full time-dependent form of the ionization balance equations. By definition, the relative density  $n_{X,i}$  of ion  $i$  of a certain element  $X$  varies with time as a function of the electron density,  $n_e$ , the recombination rate from stage  $i+1$  to  $i$  (given by the recombination coefficient  $\alpha_{X,i+1 \rightarrow i}$  times the electron density), and the ionization rate from stage  $i$  to  $i+1$ . Gathering the contribution by photoionization, Compton ionization, collisional ionization, and Auger ionization in the ionization coefficient  $\gamma_{X,i \rightarrow i+1}$ , the time-dependent ionization balance equation is written as follows (Krolik & Kriss 1995):

$$\frac{dn_{X,i}}{dt} = (n_{X,i+1}n_e\alpha_{X,i+1 \rightarrow i}) - (n_{X,i}n_e\alpha_{X,i \rightarrow i-1}) + \sum_{k=1}^{i-1} (n_{X,i-1-k}\gamma_{X,i-1 \rightarrow i}) - \sum_{k=1}^i (n_{X,i-k}\gamma_{X,i \rightarrow i+1}). \quad (1)$$

The equation represents the sum of the destruction (second and fourth terms) and formation rate (first and third terms) of each ion considering several processes of ionization and radiative recombination. The two ionization terms take into account all forms of ionization in SPEX, including the inner-shell ionization that can induce additional multiple ionizations. In the case of photoionization equilibrium, photoionization dominates over the other ionization processes, including collisional ionization.

The solution of Equation (1) defines the photoionization timescales,  $t_{\text{ph}}$ , and recombination,  $t_{\text{rec}}$ , timescales, which together measure the time necessary for plasma with density  $n_e$  to reach photoionization equilibrium with the ionizing continuum for an increasing or decreasing flux phase, respectively. For each point of the light curve of  $L_{\text{ion}}$ , these timescales can be approximated by the inverse of the destruction rate of the ion  $i$  of the element  $X$ , which define the equilibrium timescale,  $t_{\text{eq}}$  (Krolik & Kriss 1995; Nicastro et al. 1999), as

$$t_{\text{eq}}^{X^i, X^{i+1}} \sim \frac{1}{\alpha_{X, i+1 \rightarrow i} n_e} \cdot \left[ \frac{1}{-(\alpha_{X, i \rightarrow i-1} / \alpha_{X, i+1 \rightarrow i}) + (n_{X, i+1} / n_{X, i})} \right]. \quad (2)$$

Thus, the plasma will reach equilibrium with the ionizing source after a time delay  $t_{\text{eq}}$ . Equation (1) shows that the time necessary for a gas to reach equilibrium critically depends on the characteristic electron density  $n_e$  of the plasma. High-density clouds reach the photoionization equilibrium in short timescales by quickly responding to changes in the ionizing continuum. On the other hand, low-density gases need more time to achieve the ionization balance with the ionizing radiation. Especially in this late response scenario due to low-density absorbers it is important to consider the time-dependent effect in the photoionization modeling.

The behavior of the time variation of ionic abundances depends on two factors: first, the ratio  $t_{\text{eq}}/t_{\text{var}}$ , where  $t_{\text{var}}$  is the typical timescale on which most of the fluctuations in the ionizing radiation occurs. Second, it depends on the coefficient of variation (i.e., the ratio of the standard deviation to the mean) of the ionizing continuum, which quantifies the amplitude of the flux fluctuations. We describe here the time-dependent effects identifying three different scenarios:

1. *Equilibrium state*: When  $t_{\text{eq}} \ll t_{\text{var}}$  the plasma ionization state is constantly in equilibrium with the ionizing radiation. Under this condition, a large variation in the ionizing continuum would lead to a significant change in the ionization state. Either a very high-density absorber or a slowly variable ionizing source could lead to the equilibrium condition.
2. *Nonequilibrium steady state*: When  $t_{\text{eq}} \gg t_{\text{var}}$ , the ionic concentrations do not respond to the ionization flux reaching a steady state defined by the ionization and recombination states. The plasma is therefore constantly out of equilibrium with the ionizing continuum. However, if the amplitude of the source variability is small, the differences from the mean are modest. This steady-state condition is common in scenarios with either very low-density absorbers, or a rapidly variable ionizing source, or both.

3. *Delayed state*: When  $t_{\text{eq}} \sim t_{\text{var}}$ , the plasma ionic concentrations evolve smoothly and with a delay relative to the ionizing luminosity variability. The plasma is neither in equilibrium nor in a nonequilibrium steady state. This is in principle the most interesting case since the time delays between the ionization state of the plasma and the ionizing luminosity are effectively used to constrain the density of the ionizing source.

Consequently, a time-dependent photoionization analysis of plasma in an equilibrium state or in a nonequilibrium steady state will only allow us to derive, respectively, a lower and an upper bound on the gas density, which correspond to an upper and lower limit on its distance, respectively. Instead, observing the time delay on which the absorbing outflow responds to the ionizing continuum will allow constraining its location more precisely.

In order to understand which case applies to a plasma it is crucial to estimate both  $t_{\text{eq}}$  and  $t_{\text{var}}$ . In general, the power spectral density of fluctuations or the excess variance of the light curve (e.g., Nandra et al. 1997; Ponti et al. 2012) helps determine the variability of the ionizing continuum. The estimate of  $t_{\text{eq}}$  is even more complicated since according to Equation (2) it requires the knowledge of the density and ionization state (thus, the ionic concentrations,  $n_{X, i}$ ) of the absorbing plasma. In Figure 1, we show the recombination timescale, which is a good approximation of  $t_{\text{eq}}$ , as a function of the gas density assuming a typical type 1 AGN ionizing continuum. In specific, we adopt the ionizing spectral energy distribution (SED) of Mrk 509 taken from Mehdipour et al. (2011) to compute the recombination timescales. In the top panels, we display the  $t_{\text{rec}}$  of all the relevant ions of oxygen and iron for plasma with  $\log \xi = 2.0$ . The recombination timescale of different ions can vary by orders of magnitude from one ion to the next, even for ions of the same element. Different elements reach their equilibrium on different timescales.

In the bottom panels of Figure 1, we show how the recombination timescale of a single ion (O VIII and Fe XXVI) relates to the ionization state of the plasma using a grid of  $\log \xi$  spanning between  $-1$  and  $6$ . The ionization level of the plasma leads to the concentrations of the ionic species and consequently their recombination timescales. When the ionic concentrations reach their maximum (in this case,  $\log \xi \sim 2.0$  and  $\log \xi \sim 4.0$  for O VIII and Fe XXVI, respectively), the ions require a longer time to reach equilibrium. Moreover, the fact that we observe a larger scatter for O VIII with respect to Fe XXVI is due to their different ionic concentration distribution: O VIII has a broader distribution than Fe XXVI (see, for example, Figure 6 in Mehdipour et al. 2016).

Finally, when characterizing a time-evolving ionized plasma it is important to include the cooling timescale, which indicates the time necessary for a gas to cool down. As we will show in the following section, the cooling timescale has a significant impact on the time evolution of the concentration of the plasma ions.

### 3. A New Time-dependent Photoionization Model

Commonly used photoionization models are limited by the assumption that the plasma is constantly in ionization and excitation equilibrium. Therefore, they are only suitable to describe the absorbers found in the *equilibrium* case when  $t_{\text{eq}} \ll t_{\text{var}}$ . Using the standard photoionization models to

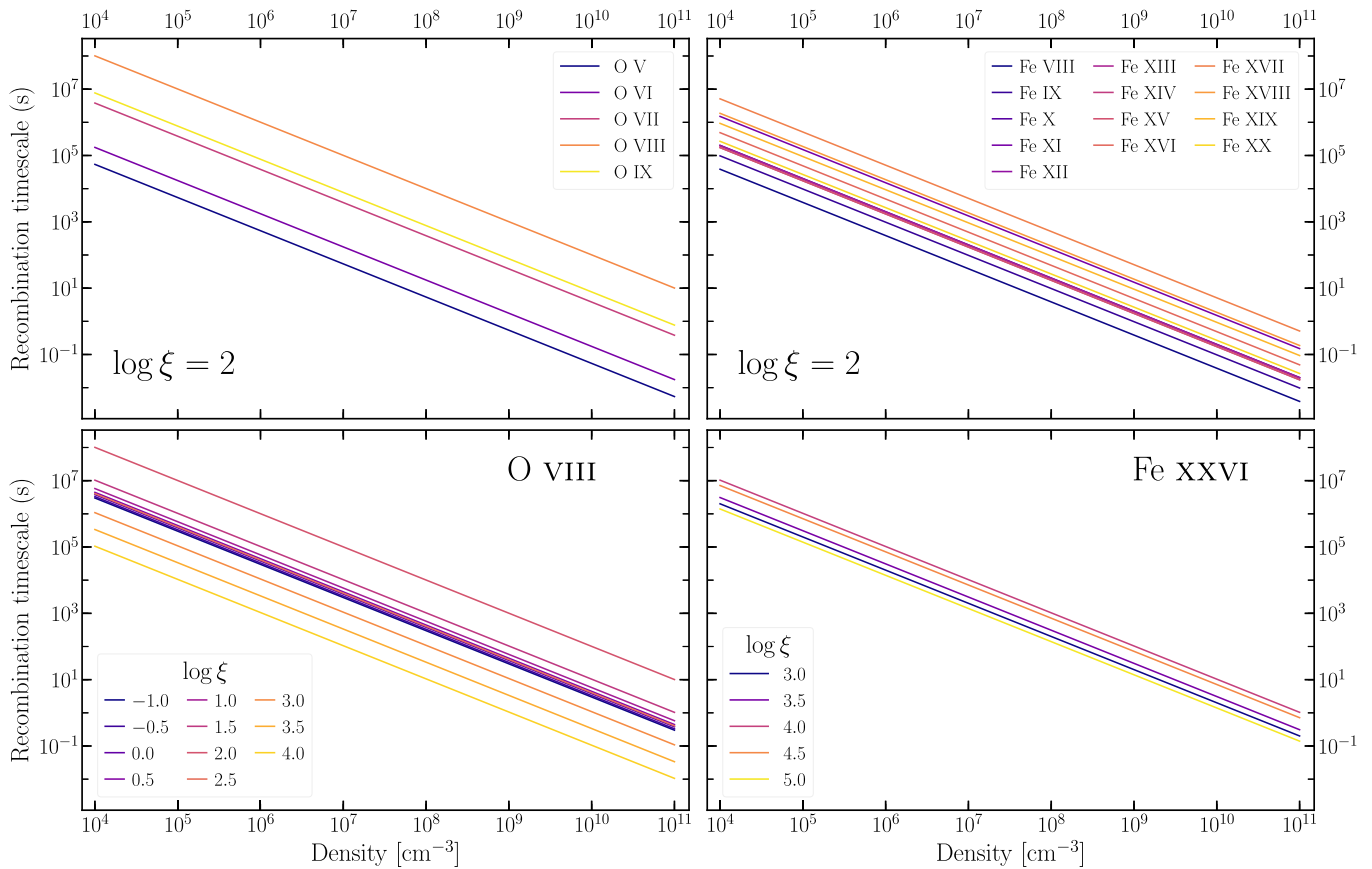


**Figure 1.** Recombination timescale as a function of the density of plasma in photoionization equilibrium. In the top panels, we show the recombination timescale of the oxygen (left) and iron (right) ions for plasma with an ionization parameter of  $\log \xi = 2$ . We show only the ions which have a relative concentration larger than  $10^{-6}$ . In the bottom panels, we display the recombination timescales of the H-like ion of oxygen (left) and iron (right) for a grid of ionization parameters.

characterize the other two scenarios described in Section 2 would lead to the wrong conclusion since the ionization state of the plasma is in non-photoionization equilibrium. In order to correctly characterize such absorbers, we developed the `tpho` model, which accounts for the time dependency of the ionizing and recombining processes that take place in a photoionized plasma together with all the relevant heating and cooling processes. The ultimate goal of this model is to determine the location of the AGN outflows and consequently their energetic properties (kinetic power, momentum outflow rate, outflow mass rate), which are crucial to understanding the AGN feedback mechanism.

In the following section, we describe the `tpho` model in detail explaining the algorithm and its inputs and outputs. Subsequently, to illustrate the time-dependent effects, we apply the model to two didactic cases characterized by a sudden increase and decrease in the ionizing luminosity (Sections 3.2 and 3.3, respectively). This simple case allows us to study how the temperature, the heating/cooling rates, and the ionic concentrations evolve when the gas is no longer assumed to be in photoionization equilibrium. We also compare the time evolution of close ions (e.g., O VIII and O IX) and ions of different elements (i.e., oxygen and iron) for different densities.

A more realistic case will be examined in Section 3.4, where we calculate the time-dependent effects introduced by a flaring light curve. This specific example highlights the three scenarios explained in Section 2 and the density range in which the model is sensitive for a given time variability. Finally, we compute the time evolution of the X-ray transmission of the

plasma and compare it with the equilibrium solution in Section 3.5 to understand the importance of the time-dependent effects in a time-resolved X-rays spectroscopy analysis.

### 3.1. TPHO Model

The `tpho` model enables a realistic characterization of the evolution of the ionization state of plasma exposed to a variable photoionizing source. The model has been implemented in the X-ray fitting code SPEX<sup>6</sup> (Kaastra et al. 1996) and released to the community with the 3.07 version of the software Kaastra et al. (2020).

The code evaluates the time evolution of all ionic concentrations for the elements with an atomic number between 1 (H) and 30 (Zn). To do so, it solves the set of  $N$ -coupled ordinary first-order differential equations shown in Equation (1), which is analytically solvable only for  $N = 2$ . We solve all these equations simultaneously using the subroutine `solcon` of SPEX, which is based on the work of Kaastra & Jansen (1993). The method consists of the calculation on the fly of the transition matrix, which contains all the ionization and recombination rates for a grid of temperatures and ionization parameters. Eigenvalues and eigenvectors of these matrices are also calculated. The ionization balance is computed at small steps according to the time evolution of ionization and temperature in the plasma. Finally, the eigenvector decomposition and the calculated coefficients are used to evaluate the ionic concentrations at each time step.

<sup>6</sup> <https://spex-xray.github.io/spex-help/index.html>

The code calculates the evolution of several heating and cooling processes: photoionization, Compton scattering and ionization, Auger electrons, free-free absorption, collisional de-excitation, and external heating for the heating rates, whereas radiative recombination, collisional ionization, inverse Compton scattering, bremsstrahlung, collisional excitation, and dielectronic recombination for the cooling rates. Cooling is assessed using the time-dependent ion abundances. The difference between the total cooling and heating processes is used to determine the temporal evolution of the plasma temperature.

The `tpho` model requires several inputs for the determination of the time evolution of the ionization balance. For the initial conditions of the plasma, the model adopts photoionization equilibrium in order to start the evolution of the plasma. The spectral shape of the ionizing continuum is also necessary to determine the photoionization rates. The `tpho` model can, like `pion`, take the SED directly from the continuum components set by the user in `SPEX`. Alternatively, the SED can be provided via an input file. The variability of the ionizing luminosity is also required to determine the time evolution of the ionic concentrations. The code uses the light curve of the ionizing luminosity to interpolate the ionization parameter. The last fundamental parameter necessary to solve the time-dependent ionization balance equations is the density of the plasma,  $n_{\text{H}}$ , which is the parameter of interest, and can be either fixed or fitted to the data in the `tpho` model.

The main outputs of the code are the ionic concentrations of all the elements, the heating/cooling rates, and the plasma temperature as a function of time. We plot the outputs of the model in the following sections for three simple cases highlighting their dependence on the gas density. The `tpho` code then uses the obtained ionic concentrations to calculate the corresponding absorption and emission spectrum of the plasma at each time step. Thus, a time-resolved spectrum taken at time  $t$ , can be fitted by applying the corresponding `tpho` spectrum that is calculated at time  $t$ .

### 3.2. Light-curve Case: Step-up Function

In order to examine the evolution of ionic concentrations calculated with `tpho`, and compare it with the equilibrium scenario (`pion`), we adopt the simplest case of a step-up function light curve. In this case, we assume that the ionizing flux goes from a *low* to a *high* state almost instantaneously ( $\Delta t \sim 0.01$  s) with a factor 10 change in flux. The light curve is shown in the upper panel of Figure 2. For the initial condition, we considered an optically thin gas cloud with an initial ionization parameter of  $\log \xi = 2$  and illuminated by the SED of Mrk 509 (Mehdipour et al. 2011). With the `tpho` model, we computed the time evolution of the ionic concentrations for a grid of hydrogen densities ranging between  $10^4$  and  $10^{10} \text{ cm}^{-3}$ .

The time-dependent behavior of the concentration of O VIII, O IX, Fe XIX, and Fe XX is shown in Figure 2. For different hydrogen densities, the ionic concentrations follow the same exponential evolution but they systematically shift over different timescales. The shift is driven by the different densities of the gas. Plotting the ionic concentration as a function of  $n_{\text{H}} \times t$  the curves will perfectly overlap (see, for example, the top panel of Figure 6).

Ions in dense gases (yellow lines) reach their equilibrium concentration faster than ions in less dense gases (blue lines). For comparison, we also calculated the ionic concentration curve for a gas in photoionization equilibrium using the `pion`

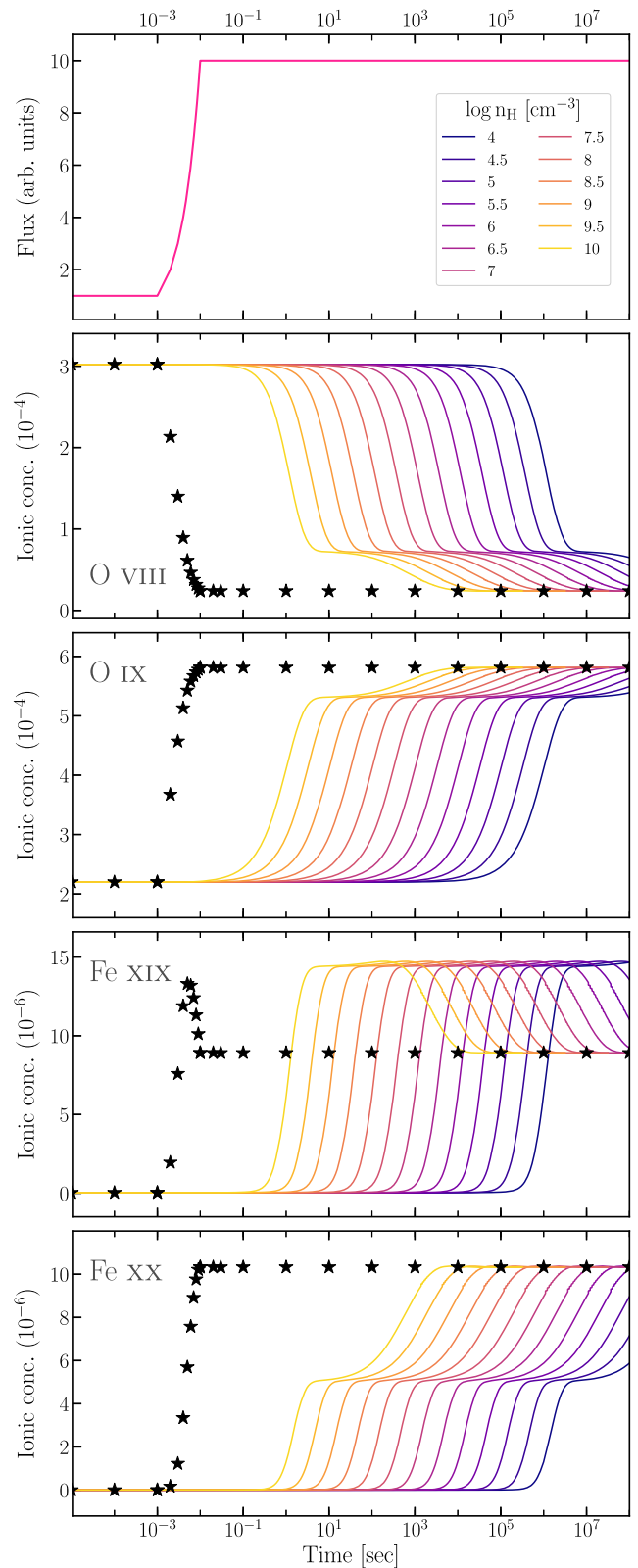


**Figure 2.** Step-up light-curve case: the light curve is shown in the top panel. The ionizing flux increases by a factor of 10 in 0.01 s. In the panels below we show the time-dependent evolution of the concentrations relative to the hydrogen of O VIII, O IX, Fe XIX, and Fe XX for different gas densities and compared it with the ionic concentrations for a plasma in photoionization equilibrium (black stars).

model (black stars). Interestingly, the evolution of the ionic concentration curves calculated with `tpho` appears different from the equilibrium one. All four ions show a flattening in

their evolution, which is closely related to the time evolution of plasma temperature.

In the top panel of Figure 3, we illustrate how the temperature of the gas evolves considering the same step-up light curve described above. When considering the time-dependent effects, the gas reaches the equilibrium temperature after a significant time delay with respect to gas in ionization equilibrium (black stars). This time delay increases with decreasing gas density. High-density gas with  $n_{\text{H}} = 10^{10} \text{ cm}^{-3}$  takes  $\sim 10$  ks to reach the equilibrium temperature whereas low-density gases ( $n_{\text{H}} < 10^6 \text{ cm}^{-3}$ ) can take a few years ( $t > 10^5$  ks) to reach the equilibrium value.

The plasma temperature is evaluated by summing the total heating and cooling rates shown in the second panel of Figure 3: the temperature increases when the heating is larger than the cooling and is constant when the two processes become equivalent. The total amount of energy injected into the plasma strongly depends on the density of the plasma. The heating curves (solid lines) increase during the jump from low to high flux level. As soon as the ionizing radiation reaches the high state, the heating rate in high-density gas starts to drop. The cooling rates (dashed lines) start out as constant, but kick in at late times. These late changes in the heating and cooling rates, alongside temperature, naturally alter the ionic concentrations, making them rise or decline, depending on the ion. Indeed, at around the time of the second decline/rise in ionic concentration shown in Figure 2, there are noticeable deviations in the total cooling/heating rates.

In the third panel of Figure 3, we compare the shapes of the heating-rate curves, which were computed fixing the initial ionization parameter of the plasma. The curves show an extended peak close to their maximum heating-rate value. The duration of this peak anticorrelates with the gas density. This shows again that denser plasmas react more quickly to incoming radiation. In the bottom panel, we show the contribution to the total of the different heating and cooling processes considered in the calculations for a gas with a density of  $n_{\text{H}} = 10^7 \text{ cm}^{-3}$ . For the considered ionizing continuum, the heating is dominated by photoionization. Auger electrons and Comptonization contribute less ( $\sim 10\%$  and  $< 1\%$ , respectively), and all the rest of the processes listed in the beginning of Section 3.1 can be neglected here. Collisional excitation, radiative recombination, and bremsstrahlung are, instead, the major cooling processes.

### 3.3. Step-down Light Curve

To compare the previous study case with a scenario where the cooling rates and the recombination processes are expected to dominate, we repeated the same investigation but for a step-down light-curve function: the ionizing continuum goes from high to low flux level by a factor of 10 (see light curve in the top panel of Figure 4). To reproduce exactly the opposite of the previous test we assumed the SED shape of Mrk 509 and an ionization parameter of  $\log \xi = 3$  as the initial condition.

In Figure 4, we show the time evolution of the O VIII, O IX, Fe XIX, and Fe XX concentrations. As shown before, the time necessary for each ionic concentration to reach its equilibrium value depends on its density. However, the ionic concentration curves do not follow the reverse pattern of the step-up light-curve case shown before (Section 3.2), as would be expected for a plasma in ionization equilibrium.

In the top panel of Figure 5, we show how the plasma temperature drops as a function of time and density. As shown

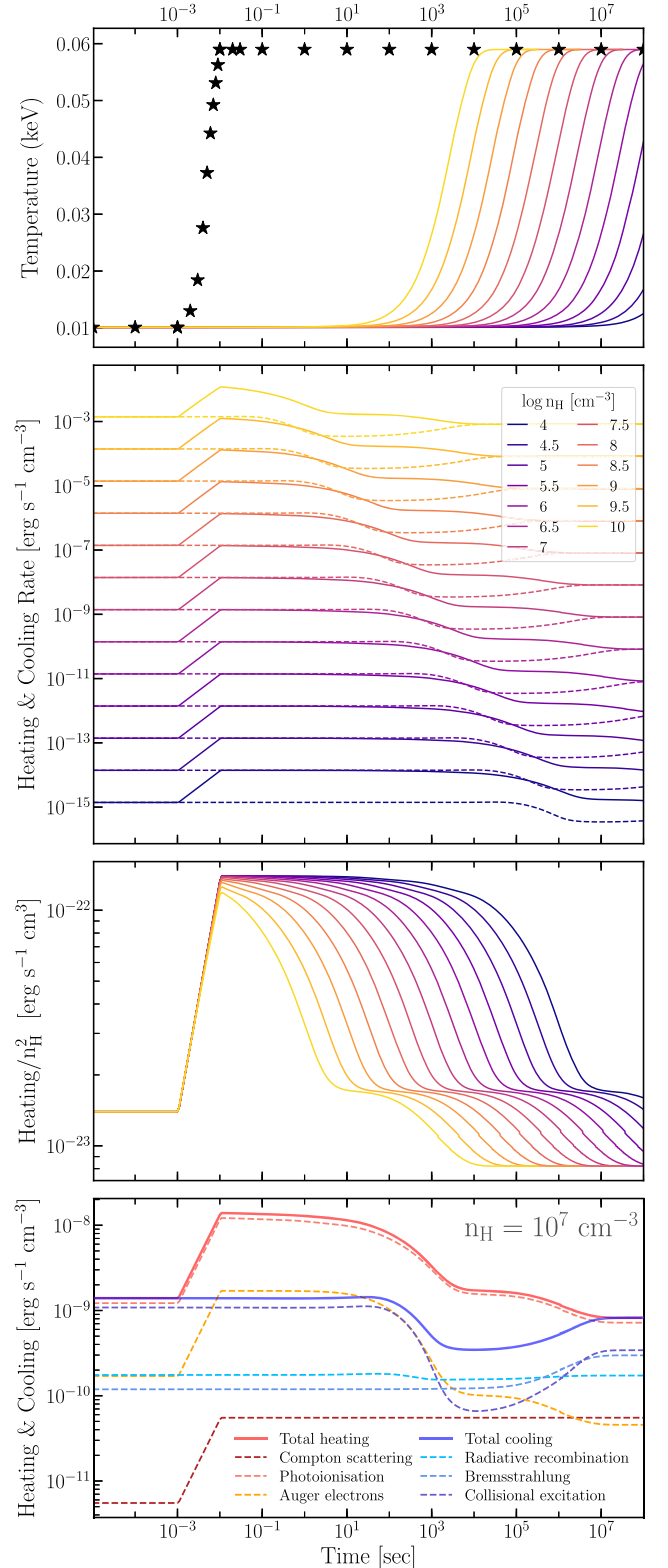


**Figure 3.** Step-up light-curve case: the first two panels show, respectively, the time-dependent evolution of the electron temperature and the heating and cooling (solid and dashed lines) rates for a grid of density values. In the third panel, we compare the shape of the heating curves dividing them by their dependency on the gas density. The bottom panel illustrates the contribution of the main heating and cooling processes for a plasma with  $n_{\text{H}} = 10^7 \text{ cm}^{-3}$ .

before, the temperature is driven by the difference between the cooling (dashed lines) and heating rates (solid lines) shown in the second panel. In this case, the cooling is larger than the

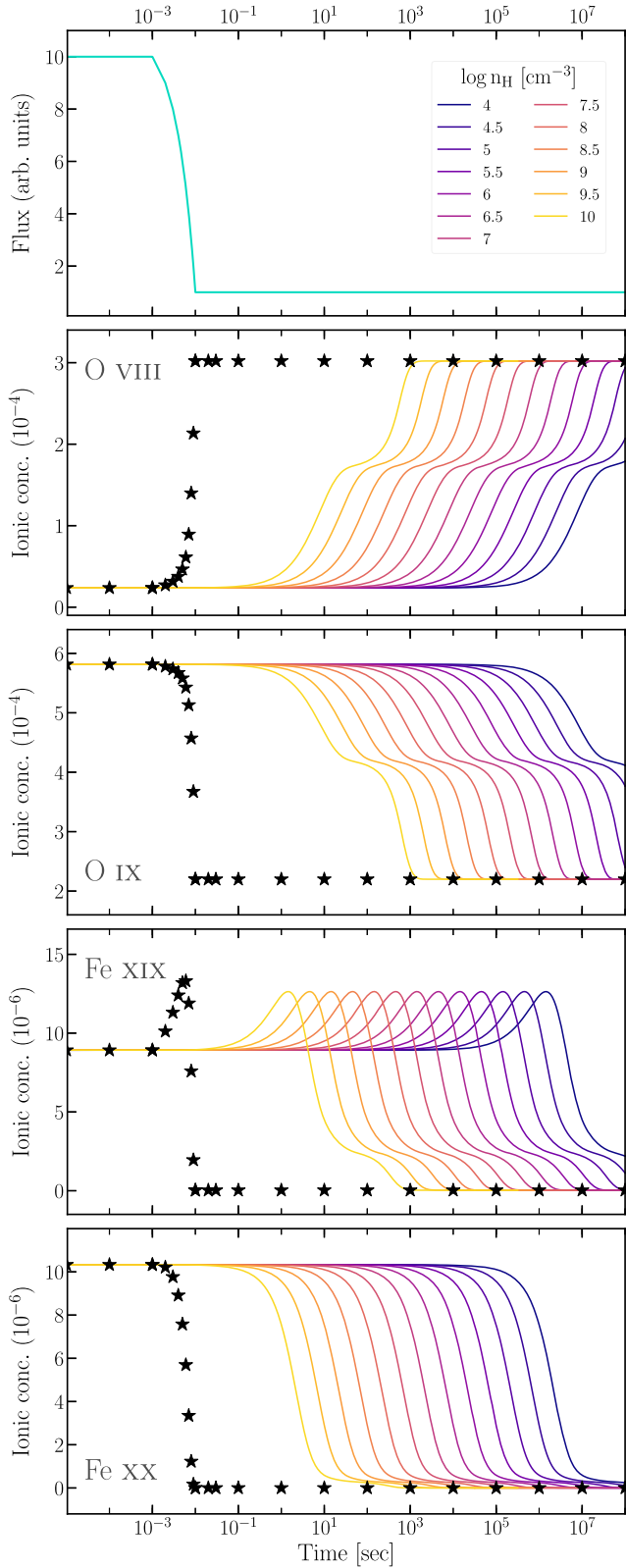


**Figure 4.** Step-down light-curve case: the light curve is shown in the top panel. The ionizing flux drops by a factor of 10 in 0.01 s. In the panels below, we show the time-dependent evolution of the concentration relative to the hydrogen of O VIII, O IX, Fe XIX, and Fe XX for different gas densities and compared with the ionic concentrations for a plasma in photoionization equilibrium (black stars).

heating and leads to the decrease in temperature. During the transition from high to low flux level, the cooling does not vary, whereas the heating rate drops. As observed in the

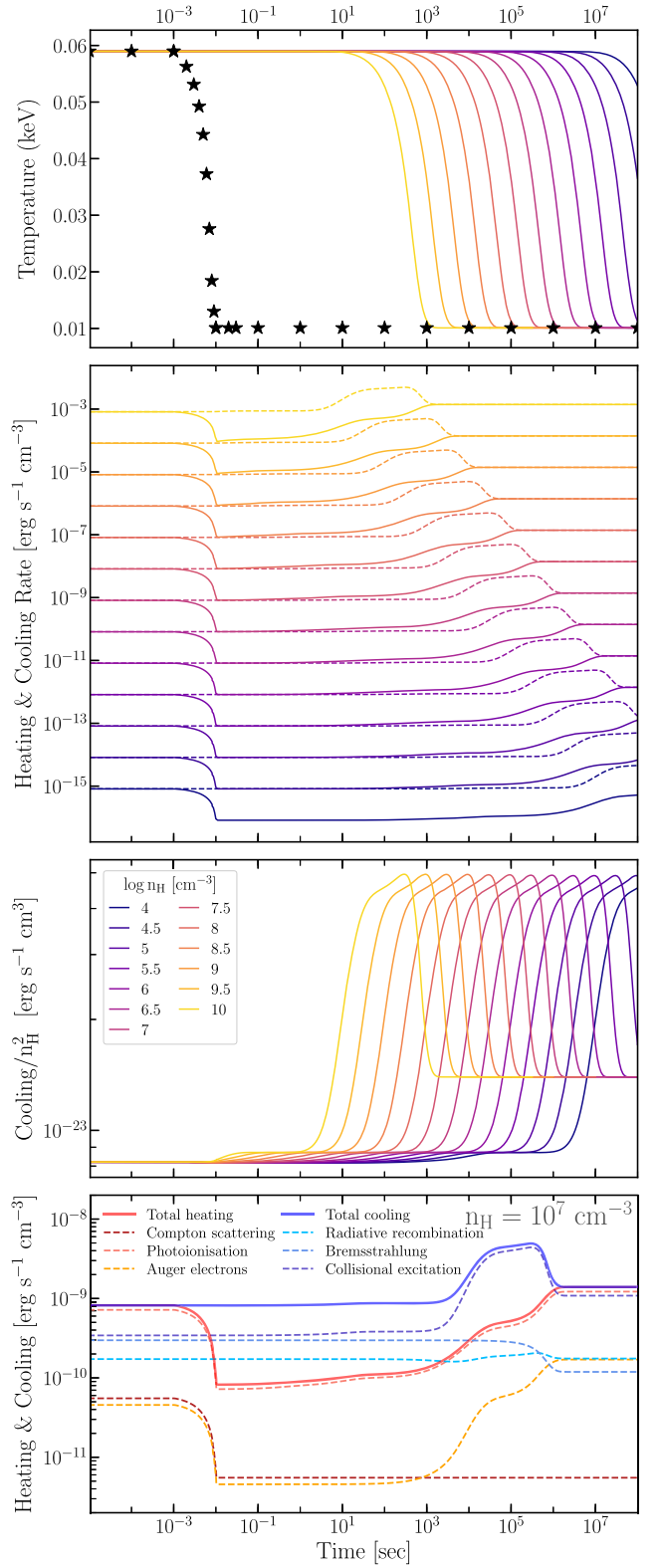


**Figure 5.** Step-down light-curve case: the first two panels show, respectively, the time-dependent evolution of the electron temperature and the heating and cooling (solid and dashed lines) rates for a grid of density values. In the third panel, we compare the shape of the cooling curves dividing them by their dependency on the gas density. The bottom panel illustrates the contribution of the main heating and cooling processes for a plasma with  $n_H = 10^7 \text{ cm}^{-3}$ .

previous case, the change in the heating always happens at the same time independent of the gas density. After this jump, both cooling and heating rates remain steady for a time period that



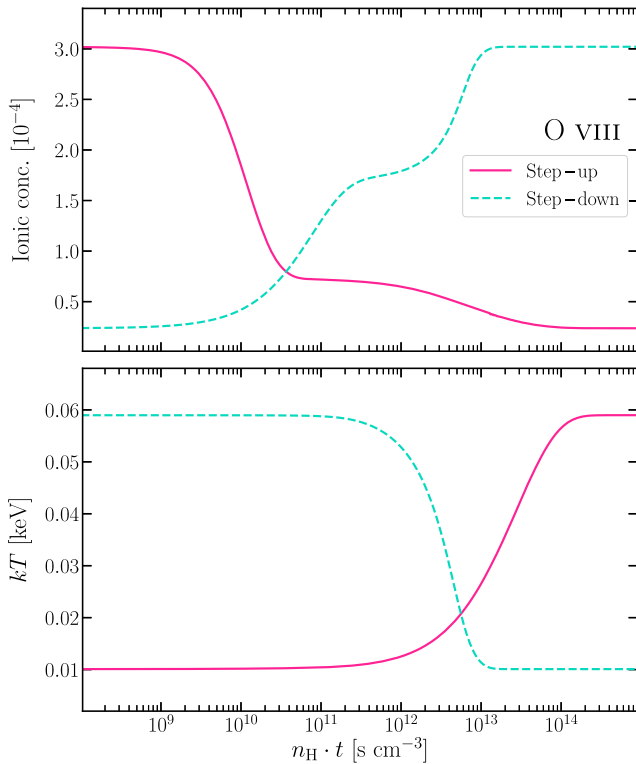


**Figure 6.** Comparison between the step-up and step-down scenarios. In the top panel, we show the evolution of the O VIII concentration as a function of  $n_{\text{H}} \times t$ . In the same rest frame, the evolution of the plasma temperature is illustrated in the bottom panel.

depends on the gas density: the lower the density, the longer the steady phase. Then, both cooling and heating increase in the same manner until the cooling finally drops, reaching the same level as the heating. From this moment on, the gas is in photoionization equilibrium with the ionizing source.

The cooling rate curve has the same shape for different densities, but they are spread over different timescales, as shown in the third panel of Figure 5. In the bottom panel, we show the total cooling rate curve for a gas with density of  $n_{\text{H}} = 10^7 \text{ cm}^{-3}$  with all the processes that contribute to it. Collisional excitation is the most important phenomenon and it is responsible for the bump observed at a later time in the total cooling curve. The ratios between the different contributions do not vary among the grid of densities considered here. Photoionization, Compton scattering, and Auger electrons are, instead, the main heating processes.

It is now possible to compare the ionization case, represented by the step-up function, with the recombination case, described by the step-down function. In the top and bottom panels of Figure 6, we juxtapose, respectively, the evolution of the O VIII concentrations and the plasma temperature as a function of  $n_{\text{H}} \times t$ . The two concentration curves follow shapes that are not the inverse of each other, as we might expect to see for a gas in photoionization equilibrium. They both include a plateau phase, which, as we have already seen in Figure 2 and Figure 4, is common to all the ionic species.

In the ionization case (solid purple line), the concentration of O VIII reaches the plateau 10 times faster than in the recombination configuration (dashed light-blue line). The duration of the plateau and the following rise (or drop) of the ionic concentration depend on the late evolution of the temperature. In the recombination case, the temperature varies

significantly quicker than in the ionization case and it reaches the equilibrium value in a shorter time. Consequently, the recombining ionic concentration shows a shorter flat phase and reaches the final equilibrium state around 10 times faster than the ionizing curve. These differences show the importance of including the computation of the plasma temperature for an accurate time-dependent modeling of a photoionized plasma.

### 3.4. Flaring Light Curve

The previous two scenarios explained in Sections 3.2 and 3.3 represent two didactic frameworks that help demonstrate the time-dependent effects on the ionic concentrations. In this section, we present a more realistic case where the ionizing continuum flares briefly as shown in the top panel of Figure 7. In detail, the ionizing luminosity increases by a factor of 10 in 6 ks (between the first red and gray vertical dashed line), stays in a high state for 3 ks (between the two gray-dashed vertical lines), and subsequently decreases to a low state again in 6 ks (between the second red and gray-dashed vertical lines).

Using this flaring light curve, the SED shape of Mrk 509, and ionization parameter  $\log \xi = 2.0$ , we computed the time evolution of the ionic concentrations. In Figure 7, we show the curves of the concentration of O VIII, O IX, Fe XIX, and Fe XX as a function of time and density. It is easy to distinguish in this case the three scenarios described in Section 2: (1) in gas with density above  $10^8 \text{ cm}^{-3}$  (yellow and orange lines) the ionic concentrations closely follow their *equilibrium* value (black stars); (2) when the density is between  $10^6 \text{ cm}^{-3}$  and  $10^8 \text{ cm}^{-3}$  (red-purple lines) the ionic concentrations are *delayed* and smooth with respect to the equilibrium curve; (3) the ionic concentrations of low-density gases, with  $n_{\text{H}} < 10^6 \text{ cm}^{-3}$  (blue lines) are *steady* and do not vary significantly with time. The gas does not have enough time to respond to the initial increase in the ionizing luminosity.

The time evolution of Fe XIX concentration follows a double-horn curve that differs from the bell shape of the other three ions illustrated. Its ionic distribution peaks during the increase and decrease phases, between which the ionic state becomes less populated in favor of Fe XX, as the ionizing flux reaches its maximum. We already saw this transition in the third plot of Figures 2 and 4 for the increasing and decreasing luminosity phases, respectively.

The time evolution of the temperature is shown in the top panel of Figure 8. Only high-density plasmas (with  $n_{\text{H}} > 10^8 \text{ cm}^{-3}$ ) significantly increase their temperature during the flare of the ionizing luminosity. Moreover, the temperature peaks at a delayed time with respect to the flare. In the middle panel, we compare the total heating and cooling for the considered density grid. In this flaring scenario, the time evolution of the heating and cooling strongly depends on the gas density. For instance, the cooling is steady for low-density gas, whereas it quickly varies in the densest plasmas. Instead, the heating rate starts to evolve similarly to the ionizing radiation as soon as we consider low-density gas. Even though we mimic a light curve where the ionizing flare is symmetric, we see that during the flare the heating time is longer than its cooling time and dominates in gas with medium and low density ( $n_{\text{H}} < 10^8 \text{ cm}^{-3}$ ). To reach their energetic equilibrium (i.e., cooling = heating), the low-density gases require a longer time than the time interval illustrated here. This explains why the cooling and heating do not match at the right end of the plot. In the bottom panel, we show the main contribution of the

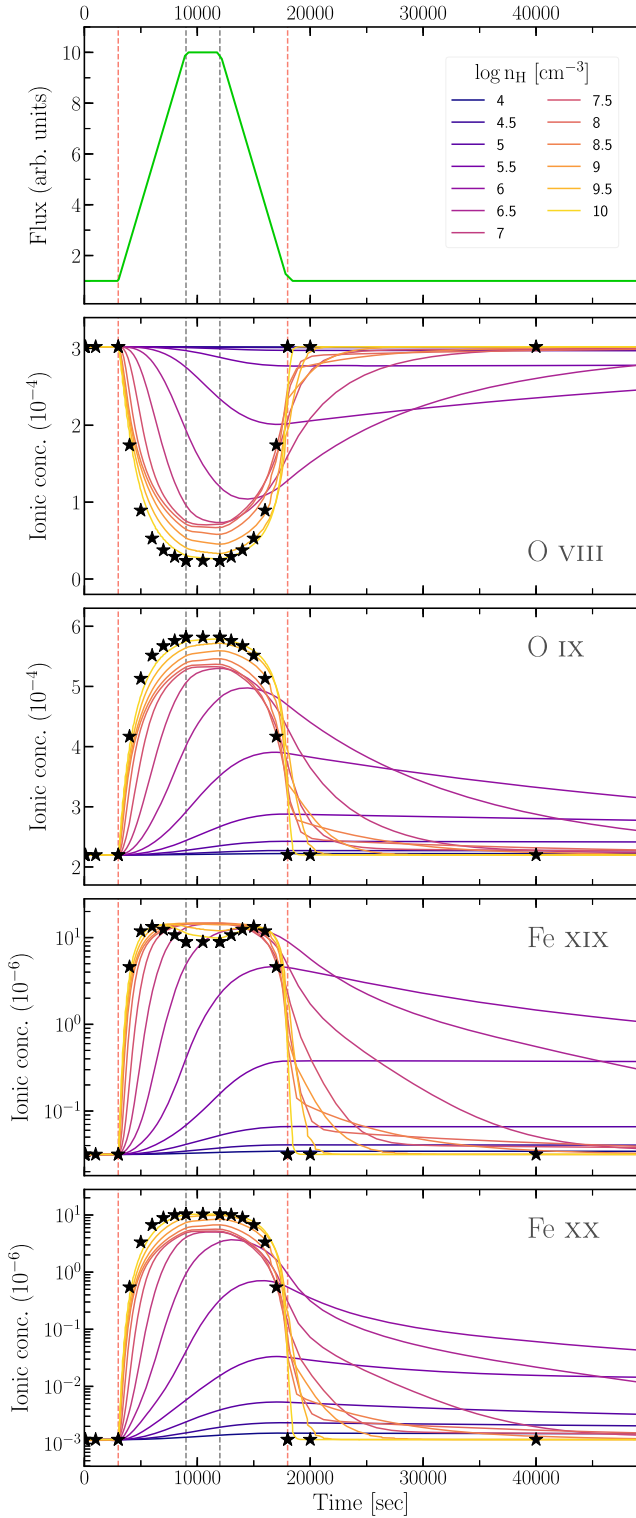


**Figure 7.** Flaring light-curve case. The light curve is shown in the top panel. The ionizing flux symmetrically increases and decreases by a factor of 10 in 3 ks. The high state phase between the dashed gray vertical lines is 2 ks long. The onset and the end of the flare are marked by two dashed red vertical lines. In the middle and bottom panels, we show the time-dependent evolution of the concentrations relative to the hydrogen of O VIII, O IX, Fe XIX, and Fe XX for different gas densities and compared it with the ionic concentrations for a plasma in photoionization equilibrium (black stars).

different processes to the heating and cooling rates. Similarly to the step-up and step-down cases studied before, photoionization is the main heating process, whereas collisional excitation

together with radiative recombination and bremsstrahlung are the most relevant cooling phenomena.

### 3.5. Transmitted Spectrum

In the final step of the `tpho` computation, all of the ionic concentrations are used to build the transmitted spectrum of the plasma. It comes as a multiplicative component and it can be used to characterize the evolution of the absorption features observed in the data. The code provides a transmitted spectrum at each desired point of the light curve, e.g., when the X-ray spectrum of the source is available. Moreover, `SPEX` allows a simultaneous fit of multiple epochs, which helps to obtain stronger constraints on the density of the absorber.

The time-dependent effects influence the spectral shape of the X-ray transmission as a function of time. In Figure 9, we compare the evolution of the transmitted spectrum for a plasma in photoionization equilibrium (in black), calculated with the `pion` model and the one calculated with the new model `tpho`, which takes into account the time-dependent effects (in magenta). We illustrate the case of the flaring light curve (see Section 3.4). For the calculation, we assumed an initial photoionization equilibrium with an ionization parameter of  $\log \xi = 1.8$  (the initial transmitted spectrum is shown by the black dotted line in the top panel), a column density of  $N_{\text{H}} = 5 \times 10^{21} \text{ cm}^{-2}$ , and a density of  $n_{\text{H}} = 10^6 \text{ cm}^{-3}$  and the SED of Mrk 509. This combination of assumptions gives a system in the *delayed* state option. We extrapolated the spectra at four different intervals of the light curve shown on the right panel: in particular, at the flare maximum (top panel), right after the flare (middle panel), and after a long period of steady state (two bottom panels).

The comparison highlights the impact of the time-dependent effect on the X-ray transmission spectrum. The deviations from the equilibrium spectrum are larger during the flare activity when the flux varies rapidly. The plasma slowly responds to the rapid increase of the ionizing luminosity and it shows a lower ionization state at the peak of the flare. The shape of the iron unresolved transitions array, which produces prominent features in the 730–830 eV energy range (15–17 Å) and the overall opacity represent the strongest differences between the two transmitted spectra in the first two extraction epochs. Before the third extraction epoch, due to the steady flux, the gas has time to recover the photoionization equilibrium and the two X-ray transmissions become similar. The gas requires a longer time ( $t \sim 75 \text{ ks}$ ) to fully recover the equilibrium (last epoch).

The density of the plasma controls the evolution of the ionic concentrations (see Figures 2, 4, and 7) and therefore the evolution of the X-ray transmission. The transmitted spectrum of lower-density gases changes slower than the one of higher-density plasma. In Figure 10, we compare the transmitted spectrum at the peak of the flaring light curve (9 ks) for several densities and two different initial ionization states ( $\log \xi = 0.5$  in the top panel and  $\log \xi = 1.8$  in the bottom panel). Regardless of the increase of the intrinsic luminosity, the X-ray transmission of gases with  $n_{\text{H}} \lesssim 10^5 \text{ cm}^{-3}$  does not diverge from the initial state (dotted black line). The equilibrium timescale for these absorbers is significantly longer than the increasing period and therefore the absorber does not have enough time to respond to the luminosity variation. In contrast, plasmas with  $n_{\text{H}} \gtrsim 10^9 \text{ cm}^{-3}$  respond almost simultaneously to the increase of the luminosity and they can be

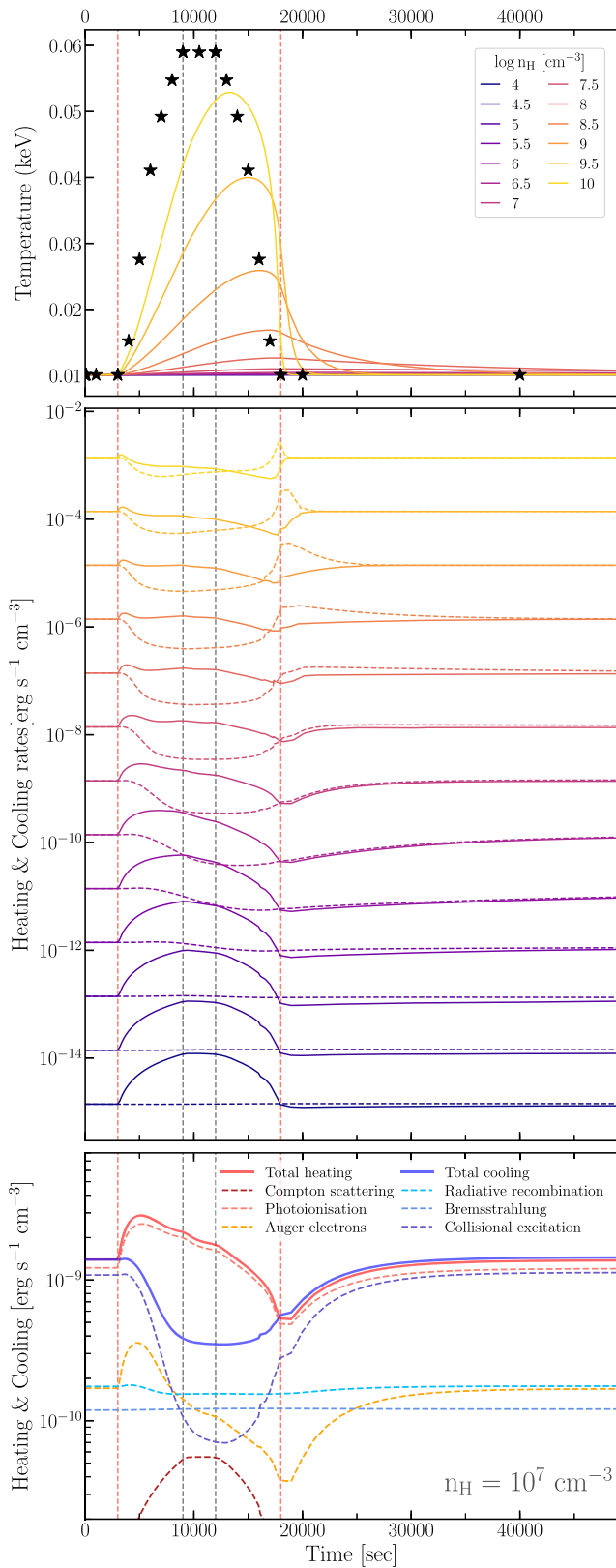


**Figure 8.** Flaring test case: the first two panels show, respectively, the time-dependent evolution of the electron temperature and the heating and cooling (solid and dashed lines) rates for a grid of density values. In the bottom panel, we display the contribution of the main heating and cooling processes for a plasma with density  $n_{\text{H}} = 10^7 \text{ cm}^{-3}$ .

considered in photoionization equilibrium (black solid line). Finally, the opacity of the plasma decreases significantly with increasing density. High-density gases can, indeed, reach higher ionization states due to their shorter equilibrium timescales.

### 3.6. Caveats

At present, our time-dependent photoionization model relies on a few assumptions. First, the model considers the plasma in photoionization equilibrium with the ionizing luminosity at the starting point of the light curve ( $t = 0$ ). This assumption is necessary to evaluate the temperature, the initial ionic concentrations, and the heating and cooling rates of the plasma. However, it is possible that an AGN outflow, for example, it is already in nonequilibrium with the X-ray emission at the beginning of the observing campaign. This can introduce uncertainties on the response time of the plasma and consequently also on its inferred density. In order to limit this uncertainty, it is important to monitor the intrinsic luminosity for an extended time interval. The initial equilibrium can be placed after a long phase of steady flux where the ionized plasma is most likely in photoionization equilibrium.

Moreover, we neglect any change in the SED components such as the power-law slope, extent of the soft excess, reflection, or the optical/UV bump during the considered time. The shape of the SED is kept frozen during the calculation of the ionic concentration evolution. Only the total normalization varies in correspondence with the ionizing luminosity. Therefore, the model is particularly suitable to describe the time-dependent effects of AGN that do not show a strong variability in the SED shape.

Differences in the ionizing SED have a direct impact on the ionizing balance and the thermal stability of photoionized plasmas (Mehdipour et al. 2016). However, the changes in the transmitted spectrum are limited to small changes in the ionizing SED. In Figure 11, we compare the transmitted spectra considering (orange) and ignoring (black) any variation in the spectral shape. In detail, we let the power-law index,  $\Gamma$  increasing by 20% (from 1.9 to 2.3) and calculated the transmitted spectrum at the flaring peak ( $t = 9 \text{ ks}$ , see Figure 9). We assumed a density of  $n_{\text{H}} = 10^6 \text{ cm}^{-3}$  and an initial ionization parameter of  $\log \xi = 1.8$ . The deviation between the two models is shown in percentage in the bottom panel. The discrepancies are within 5%, which can be neglected with the current high-resolution X-ray spectrometers. In a future version of the code, we will implement a more sophisticated algorithm able to take into account any change in the ionizing SED.

We consider only the optically thin slab of plasma where the propagation time of the X-ray radiation is smaller than both the source variability timescale and the associated recombination timescale (see Schwarz et al. 1972; Binette 1988). We neglect any time dependence of the radiative transfer, which becomes important for optically thick plasma (see García et al. 2013). Recently, Sadaula et al. (2022) extensively studied the evolution of the ion fraction and temperature at various depths in the cloud solving the time-dependent radiative transfer equation. They show the relevance of this effect for clouds with a thickness of  $10^{16-17} \text{ cm}$ . We refer to their work for a detailed

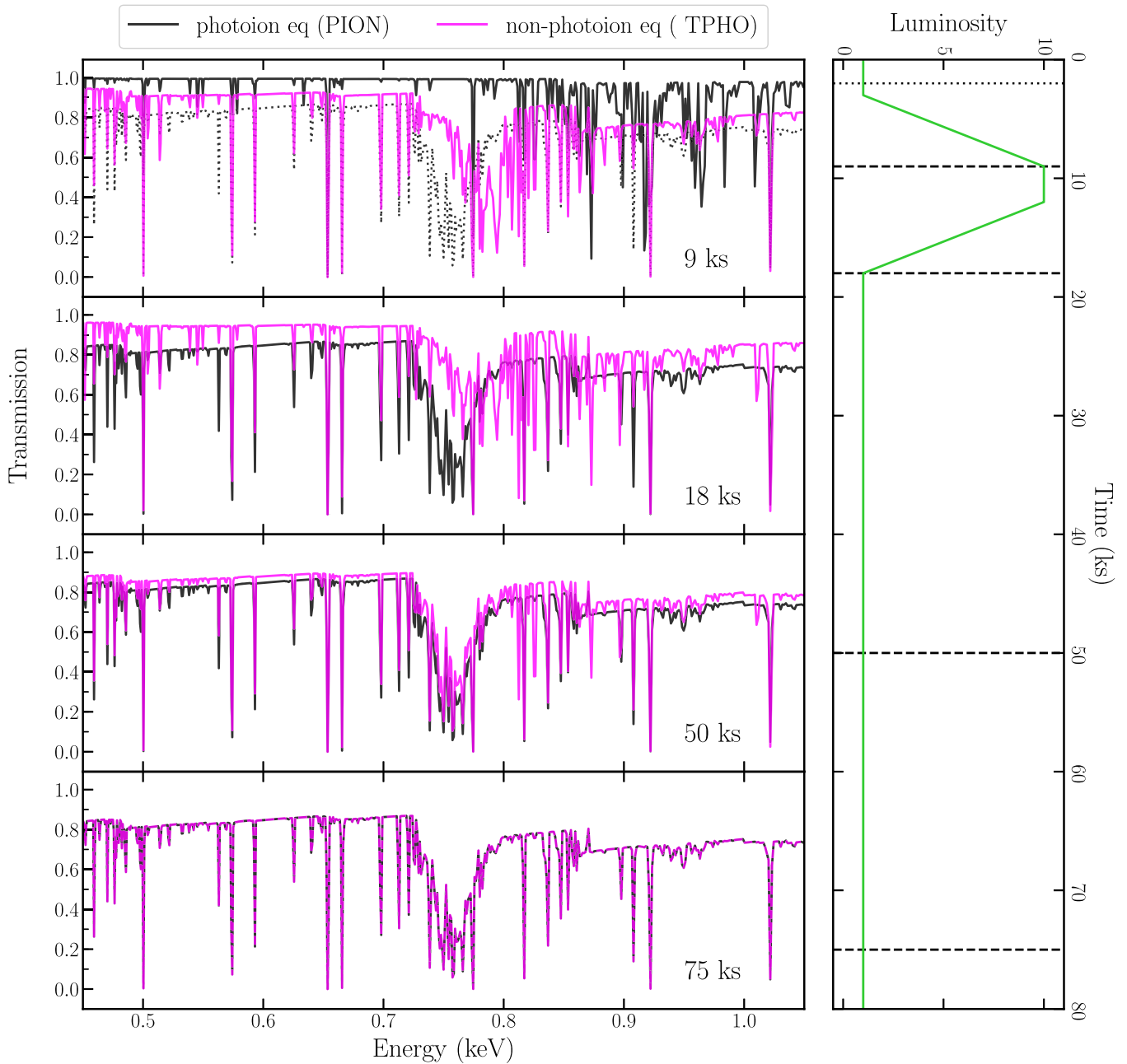


**Figure 9.** Comparison between the X-ray transmission (line and continuum absorption) of a plasma in photoionization equilibrium (black solid line) and in non-photoionization equilibrium (magenta solid line). We assume a plasma with a density of  $n_{\text{H}} = 10^6 \text{ cm}^{-3}$  and an initial ionization parameter of  $\log \xi = 1.8$ . We show a comparison at three different epochs: from top to bottom 9, 18, 50, and 75 ks, which correspond to the black dashed lines in the light-curve panel on the right. In the top panel, we also plot the initially transmitted spectrum (black dotted line), right before the onset of the flare.

comparison between the time-dependent effects of ionization balance and the ones of the radiative transfer.

Finally, the present model assumes that all ions are in their ground state. This is good enough as far as total time-dependent ionization/recombination rates are computed. At high density, many of the levels of ground terms and configurations become populated by collisions leading to population of metastable levels (Kallman et al. 2021). The critical density leading to population of the excited levels is  $\sim 10^{14} \text{ cm}^{-3}$  (Mauche et al. 2004). For higher densities this would give obviously some deviations in the computed time-dependent ion concentrations, but not by large amounts since the main effect of the density is setting the proper timescales. Level populations are not

computed because that requires much more computational effort. Thus, for higher densities, the ion concentrations are reasonable, but obviously care should be taken with the absorption spectra (which are computed assuming all ions are in the ground state).

#### 4. Discussion

Standard photoionization models such as SPEX, CLOUDY (Ferland et al. 2017), and XSTAR (Bautista & Kallman 2001) allow us to characterize astrophysical plasma in ionization equilibrium. This equilibrium assumption is valid in presence of a steady ionizing luminosity or when modeling high-density plasmas. A sudden variation of the ionizing luminosity can

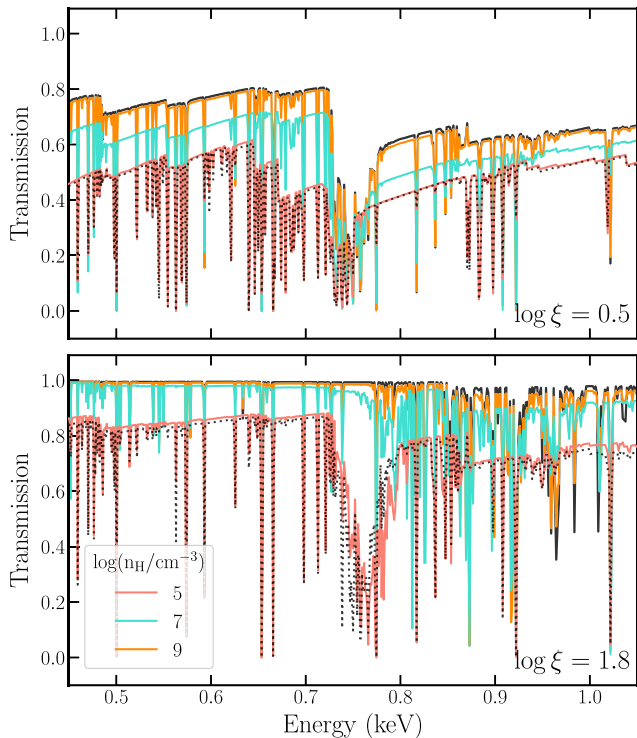


**Figure 10.** X-ray transmission of an absorber assuming different densities ( $10^5 \text{ cm}^{-3}$  in red,  $10^7 \text{ cm}^{-3}$  in turquoise, and  $10^9 \text{ cm}^{-3}$  in orange) and initial ionization parameters ( $\log \xi = 0.5$  top panel and  $\log \xi = 1.8$  bottom panel). We extracted all the spectra at the peak of the flaring light curve ( $t = 9$  ks, see Figure 9). In both panels, we overplot the initially transmitted spectrum ( $t = 0$ , black dotted line) and the spectrum of a plasma in photoionization equilibrium with the ionizing source at  $t = 9$  ks (black solid line).

cause a departure from the photoionization equilibrium. The equilibrium timescale (see Equation (2)) indicates the time necessary for the plasma to recover the ionization balance. When this timescale is similar to or longer than the ionizing source variability timescales the gas is nonequilibrium photoionization with the ionizing radiation. In other words, the assumption that heating and cooling rates are equal is not valid anymore and time-dependent effects should be taken into account (e.g., Krolik & Kriss 1995; Nicastro et al. 1999).

`tpho`, our new photoionization model based on `pion`, includes the time dependence of all ionizing/heating and recombining/cooling processes in the plasma. The model is able to characterize the ionization state of a plasma photoionized by a variable source. The full atomic database of SPEX is used to calculate the evolution of all the ionic species by solving the differential Equation (1).

Earlier time-dependent photoionization codes used only limited atomic data to study the evolution of absorption features of low-resolution X-ray spectra. For example, Nicastro et al. (1999) characterized the high signal-to-noise ROSAT observation of the Seyfert I galaxy NGC 4051 omitting photoionization from the L shell and all the iron ions. This introduced uncertainties on the computation of the abundance balance of low ionized gases and a possible overestimation of the O and Ne K shell photoionization. Morales et al. (2000) studied the complex time behavior of the oxygen absorption features detected in the ASCA and BeppoSAX spectra of MCG-6-30-15 using the code developed by Reynolds (1996) limited to only oxygen ions. High-resolution Chandra/HETG (Canizares et al. 2005) and XMM-Newton/RGS (den Herder

et al. 2001) spectra require an extended atomic model in order to analyze the variability of the whole forest of absorption lines. To study the variability of the absorbers along the line of sight of Mrk 509, Kaastra et al. (2012) used CLOUDY to generate several time-dependent photoionization models for a grid of densities.

By implementing our `tpho` model for the SPEX package we not only have direct access to the SPEX database and photoionization routines, but we can generate the transmitted spectrum, which can be promptly multiplied with the broadband model. As a result, it is possible to directly fit the data and constrain the density of the absorber. The model is therefore suitable to study the time behavior of the absorption features detected in the high-resolution spectra taken with current and future X-ray missions.

It is also possible to extend the time-dependent photoionization modeling to high-resolution spectra in the UV band (e.g., Arav et al. 2020). In case the absorber has spectral features in both the UV and X-ray band and both spectra are available, a simultaneous UV/X-ray analysis would accurately determine the time-dependent properties of the plasma. Finally, the `tpho` model can be used to verify the density estimates from metastable lines in both the UV and X-ray energy bands.

The primary scientific targets of the `tpho` model are the outflows observed in bright Seyfert I galaxies. The code allows studying the time behavior of both low and high-ionization plasma, tuning their flow and dispersion velocities, relative abundances, and column density. The main information we can access with the `tpho` model is the density of the absorber. The time-dependent effects strongly depend on this quantity (see Section 2). Consequently, by reliably deriving the density of the plasma, it is possible to accurately locate the outflows and derive their energetics.

Moreover, the time variable spectra provided by `tpho` can be used to predict the effect of warm absorber or obscuration events on the time lags and coherence of the energy-dependent light curves. The response of the gas to changes in the ionizing continuum can indeed introduce additional lags (Silva et al. 2016). Thus, recognizing the contribution of the recombining gas to the AGN X-ray time lags is crucial to interpret the continuum lags connected to propagation and reflection effects in the inner emitting regions. Recently, Juráňová et al. (2022) demonstrated that the gas response to the source radiation results in a decrease of the coherence in the Fourier timing analysis, which can be used to constrain the gas density, therefore introducing a new methodology to derive the location of outflows.

Tidal-disruption events (TDEs) and gamma-ray bursts (GRBs) represent two potential astrophysical systems where a time-dependent photoionization modeling can be applied. In these transient events, the drastic increase in luminosity photoionizes the surrounding gas (either ejecta or host galaxy); the explosive phase is then followed by a rapid decrease in the flux where the gas recombines on timescales determined by the density. The variability study of the absorption features in the spectra of such extreme events is, however, limited by the collecting area and the slew capability of current X-ray telescopes. Absorption lines are hardly detected even in the X-ray spectrum of the brightest GRBs (Campana et al. 2016) and only a few luminous TDEs show spectral features imprinted by an outflow (Miller et al. 2015). Future X-ray missions, in particular Athena, will likely enable time-dependent

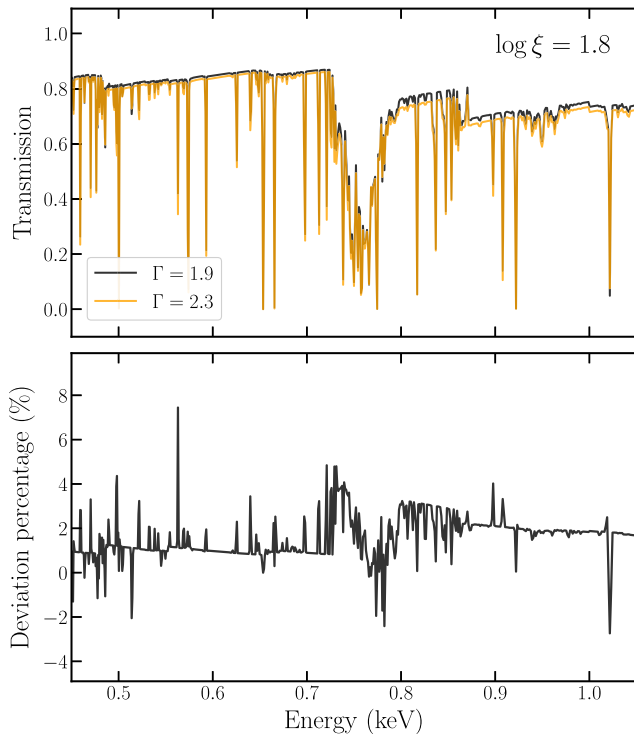


**Figure 11.** Impact of the ionizing SED on the transmitted spectrum. In the top panel, we compare the X-ray transmission of two plasmas with a different ionizing SED and with the same initial ionizing parameter and density: the black line represents the transmittance for a plasma that does not vary the SED shape; instead, the yellow line shows the transmittance of a gas that sees an increase of the power-law index by 20%. The deviation between the two models is shown in the bottom panel.

photoionization modeling of these extreme astrophysical events (Piro et al. 2021).

#### 4.1. Simulation

We discuss here the impact of the time-dependent effects on a standard time-resolved X-ray spectroscopy campaign of AGN outflows. In Figure 10, we demonstrate how the shape of the transmission spectrum of a warm absorber calculated with our `tpho` model strongly diverges from the equilibrium one depending on the density of the plasma. We now investigate how well a standard photoionization model can describe the spectral features of a gas in nonequilibrium with the ionizing source. We aim to answer the question: is a time-dependent photoionization model really necessary to fit the AGN outflow spectra?

To address this question, we simulated the absorbed spectrum of an AGN after a sudden increase in the intrinsic luminosity by a factor of 10. Specifically, we used the step-up light curve presented in the top panel of Figure 2 and we extracted the spectrum computed by our `tpho` model at  $t = 25$  ks after the jump. As for the initial conditions, we assumed the SED of Mrk 509 and a warm absorber with density  $n_{\text{H}} = 10^5 \text{ cm}^{-3}$ , column density  $N_{\text{H}} = 5 \times 10^{21} \text{ cm}^{-2}$ , ionization parameter  $\log \xi = 1$ , and outflow velocity  $v_{\text{out}} = -300 \text{ km s}^{-1}$ . We simulated the signal-to-noise ratio expected for a 50 ks observation taken with XMM-Newton/RGS. The synthetic spectrum contains the time-dependent effects and is shown in the upper left panel of Figure 12. Following the common photoionization modeling procedure, we fit the absorption features of the warm absorber adding a `pion`

component and setting the  $N_{\text{H}}$ ,  $\log \xi$ , and  $v_{\text{out}}$  as free parameters. The best fit, shown with a solid red line, favors a warm absorber component with a higher ionization parameter of 1.6. We obtained a worse statistic ( $\Delta C - \text{stat} = 60$ ) and significant residuals around the iron UTA, as shown in the left bottom panel. To correct for these residuals we added a second `pion` component (best fit in green). The fit statistic improved by  $\Delta C - \text{stat} = 22$  for three free parameters and two absorbers with  $\log \xi$  of 1.3 and 2.0 and similar column density are found. It is thus important to include the time-dependent effects in the photoionization modeling of AGN outflow.

For modeling extremely variable sources, time-independent photoionization models may not be sufficiently accurate. In some cases, they might erroneously indicate the presence of a larger number of absorber components with respect to a time-dependent photoionization analysis. As we have shown in Section 3.1, the ionic concentrations follow different time evolutions based on the density and ionization state of the gas. Thus, during specific epochs (e.g., after a strong variation in the intrinsic luminosity), it is not possible to reproduce the spectrum of gas in nonequilibrium with a standard photoionization modeling and the best fitting would show residuals around some spectral features. These discrepancies will become more significant with the advent of the new generation of high-resolution X-ray instruments.

We repeat the same analysis using the up-to-date response matrix of the mission concept Arcus, which is expected to reach a resolving power of  $R = 3800$  in the wave band 10–60 Å and an effective area of 325 cm<sup>2</sup> at 19 Å. To simulate the response of the instrument, we followed the detailed guide<sup>7</sup> written by the Arcus team. Due to its large effective area (325 cm<sup>2</sup> at 19 Å) and resolution power in the soft X-ray band ( $R = 3800$ ), Arcus would represent a powerful instrument to study how AGN outflows respond to any luminosity variation. It will revolutionize current photoionization modeling approaches as Chandra and XMM-Newton did in the early 2000s.

In the top right panel of Figure 12, we show the Arcus synthetic spectrum computed using the same setup and exposure time described above. The plot of the residual shows a strong discrepancy in the Fe UTA band, which neither a single nor a multi-steady-state component can reproduce. By not including the time-dependent effects in the modeling, the  $C$ -statistics of the best-fit decrease by  $\Delta C - \text{stat} \sim 1600$ . In presence of a variable photoionizing source, it will be crucial to include the time-dependent effects in the modeling of the absorbing plasma.

The X-ray Imaging and Spectroscopy Mission (XRISM; Tashiro et al. 2018) represents the next high-resolution X-ray telescope to be launched in 2023. The soft band of the synthetic spectrum obtained with the X-ray microcalorimeter Resolve (Ishisaki et al. 2018) is shown in 13. Similarly to the previous cases, `pion` cannot correctly characterize the absorption features linked to an ionized outflow that is in a nonequilibrium photoionization state. The statistic of the best fit decreases by  $\Delta C - \text{stat} \sim 900$  with respect to the best fit obtained with `tpho`. In this case, adding a second `pion` component significantly improves the overall best fit ( $\Delta C - \text{stat} \sim 170$ ) as the residual highlights in the bottom panel of Figure 13.

<sup>7</sup> <http://www.arcusxray.org/responses/OverallGuide.pdf>

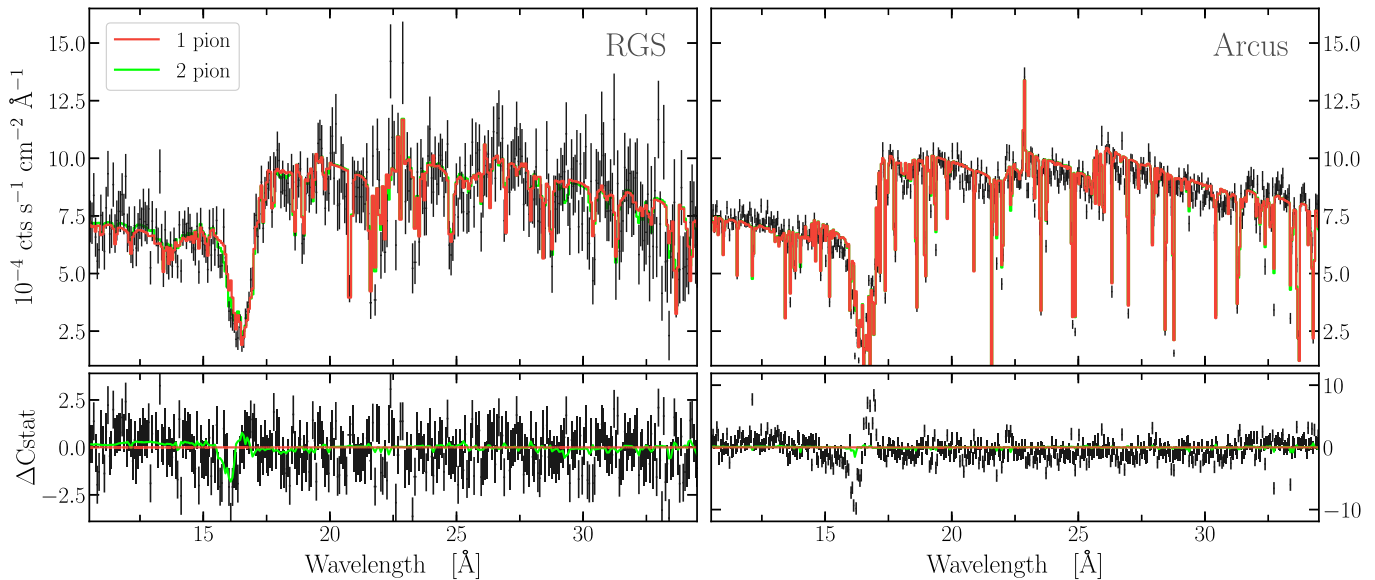


**Figure 12.** Time-dependent effects in a synthetic RGS and Arcus spectra of an AGN (SED from Mrk 509) with a warm absorber in absorption. To simulate the data we computed the time-dependent photoionization model 25 ks after a sharp increase in the ionizing luminosity. In red, we show the best fit using a `pion` component and neglecting the time-dependent effects. The residuals are displayed in the bottom panels. The best fit using two `pion` components is shown in green.

## 5. Summary

Density represents a crucial physical quantity in modeling of photoionized plasmas and ascertaining the energetics of AGN outflows. In general, standard photoionization models that assume a gas in constant ionization equilibrium do not take into account time-dependent effects in the plasma. In the present work, we have shown the impact of the density on the ionization state of a gas photoionized by a variable source. Each ion has specific recombination and photoionization timescales, which depend on both the ionization state of the plasma and its density. When the gas is not in ionization balance, i.e., when the  $t_{\text{eq}} \lesssim t_{\text{var}}$ , the shape of the transmitted spectrum is significantly affected by the time-dependent photoionization effects.

We developed a new time-dependent photoionization model, `tpho`, which has already been implemented and publicly released with `SPEX` v. 3.07. The model reads as input the light curve and the ionizing SED and computes the time evolution of the ionic concentrations and transmitted spectrum of a specific plasma ( $n_{\text{H}}$ ,  $\log \xi$ ,  $N_{\text{H}}$ ,  $v_{\text{out}}$ ,  $v_{\text{turb}}$ ). The primary goals of `tpho` are:

1. *To characterize the time-dependent effects.* We demonstrated that in presence of a variable ionizing source if the time-dependent effects are taken into account the warm absorber spectral features can be explained by a single component instead of multiple steady-state phases. Implementing the time-dependent effects in the photoionization modeling of AGN outflow is essential with the advent of new X-ray missions (e.g., XRISM and Arcus).
2. *To constrain the absorber density and location.* Knowing the distance of the different absorbing clouds from the ionizing source enables us to map the AGN outflows and determine their energetics. Applying the `tpho` model to a sample of bright Seyfert I galaxies that show the presence of outflows can provide important insights into the AGN feedback driven by the outflows and possibly understand the relation between ultrafast outflows, warm absorbers, and molecular outflows.

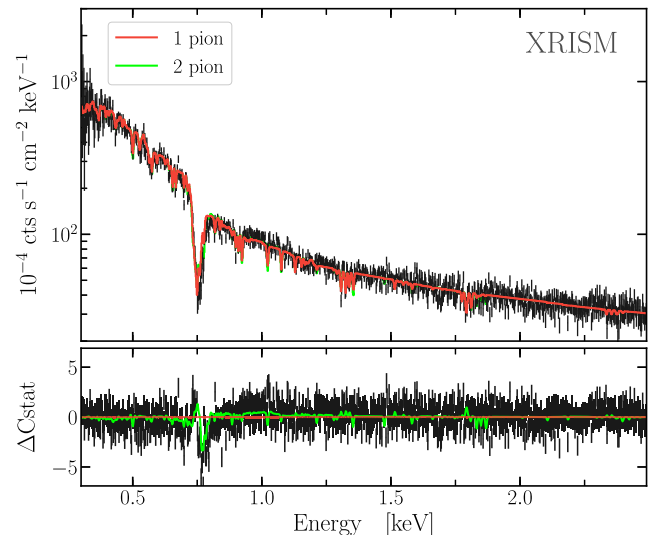


**Figure 13.** Time-dependent effects in a synthetic XRISM spectra of an AGN (SED from Mrk 509) with a warm absorber in absorption. To simulate the data, we computed the time-dependent photoionization model 25 ks after a sharp increase in the ionizing luminosity. In red, we show the best fit using a `pion` component and neglecting the time-dependent effects. The residuals are displayed in the bottom panels. The best fit using two `pion` components is shown in green.

Future X-ray telescopes will allow accurate time-dependent photoionization modeling of plasma in the presence of variable ionizing sources. In particular, low-density, ionized outflows of variable AGN will require a model that is able to characterize the time effects. Long monitoring campaigns of bright Seyfert I galaxies will not only help map the outflows along the line of sight but also help better understand their launch mechanism and estimate the mass and energy that they carry.


We thank the referee for their useful suggestions and comments. D.R. is grateful to Peter Kosec, Dave Huenemoerder, and Claude Canizares for insightful discussions. D.R. also thank Moritz Guenther for his support on the Arcus simulation.

D.R. is supported by NASA through the Smithsonian Astrophysical Observatory (SAO) contract SV3-73016 to MIT for Support of the Chandra X-Ray Center (CXC) and Science Instruments. The CXC is operated by the Smithsonian Astrophysical Observatory for and on behalf of NASA under contract NAS8-03060. The research leading to these results received funding from the European Unions Horizon 2020 Program under the AHEAD2020 project (grant agreement No. 871158). E.K. acknowledges XRISM Participating Scientist Program for support under NASA grant 80NSSC20K0733.

*Software:* The `tpho` model has been implemented in the X-ray fitting program `SPEX` v3.07 (Kaastra et al. 2020).

### ORCID iDs

Daniele Rogantini  <https://orcid.org/0000-0002-5359-9497>

Missagh Mehdipour  <https://orcid.org/0000-0002-4992-4664>

Elisa Costantini  <https://orcid.org/0000-0001-8470-749X>

Anna Juráňová  <https://orcid.org/0000-0002-7292-6852>

Erin Kara  <https://orcid.org/0000-0003-0172-0854>

### References

- Arav, N., Chamberlain, C., Kriss, G. A., et al. 2015, *A&A*, 577, A37
- Arav, N., Xu, X., Kriss, G. A., et al. 2020, *A&A*, 633, A61
- Bautista, M. A., & Kallman, T. R. 2001, *ApJS*, 134, 139
- Behar, E., Peretz, U., Kriss, G. A., et al. 2017, *A&A*, 601, A17
- Behar, E., Rasmussen, A. P., Blustin, A. J., et al. 2003, *ApJ*, 598, 232
- Behar, E., Sako, M., & Kahn, S. M. 2001, *ApJ*, 563, 497
- Binette, L. 1988, in *Active Galactic Nuclei*, ed. H. R. Miller & P. J. Wiita, Vol. 307 (Berlin: Springer), 185
- Blandford, R., Netzer, H., & Woltjer, L. 1990, in *Active Galactic Nuclei: Saas-Fee Advanced Course 20. Lecture Notes 1990*. Swiss Society for Astrophysics and Astronomy, XII, ed. T. J.-L. Courvoisier & M. Mayor (Berlin: Springer-Verlag)
- Blustin, A. J., Page, M. J., Fuerst, S. V., Branduardi-Raymont, G., & Ashton, C. E. 2005, *A&A*, 431, 111
- Campana, S., Braito, V., D'Avanzo, P., et al. 2016, *A&A*, 592, A85
- Canizares, C. R., Davis, J. E., Dewey, D., et al. 2005, *PASP*, 117, 1144
- Collinge, M. J., Brandt, W. N., Kaspi, S., et al. 2001, *ApJ*, 557, 2
- Costantini, E., Kaastra, J. S., Arav, N., et al. 2007, *A&A*, 461, 121
- Crenshaw, D. M., Kraemer, S. B., & George, I. M. 2003, *ARA&A*, 41, 117
- den Herder, J. W., Brinkman, A. C., Kahn, S. M., et al. 2001, *A&A*, 365, L7
- Ebrero, J., Domček, V., Kriss, G. A., & Kaastra, J. S. 2021, *A&A*, 653, A125
- Ebrero, J., Kaastra, J. S., Kriss, G. A., et al. 2016, *A&A*, 587, A129
- Fabian, A. C. 2012, *ARA&A*, 50, 455
- Ferland, G. J., Chatzikos, M., Guzmán, F., et al. 2017, *RMxAA*, 53, 385
- Fiore, F., Feruglio, C., Shankar, F., et al. 2017, *A&A*, 601, A143
- García, J., Elhoussieny, E. E., Bautista, M. A., & Kallman, T. R. 2013, *ApJ*, 775, 8
- Gaspari, M., Tombesi, F., & Cappi, M. 2020, *NatAs*, 4, 10
- Ishisaki, Y., Ezoe, Y., Yamada, S., et al. 2018, *JLTP*, 193, 991
- Juráňová, A., Costantini, E., & Uttley, P. 2022, *MNRAS*, 510, 4225
- Kaastra, J. S. 2017, *AN*, 338, 146
- Kaastra, J. S., Detmers, R. G., Mehdipour, M., et al. 2012, *A&A*, 539, A117
- Kaastra, J. S., & Jansen, F. A. 1993, *A&AS*, 97, 873
- Kaastra, J. S., Kriss, G. A., Cappi, M., et al. 2014, *Sci*, 345, 64
- Kaastra, J. S., Mewe, R., & Nieuwenhuijzen, H. 1996, in *11th Colloq. on UV and X-ray Spectroscopy of Astrophysical and Laboratory Plasmas*, ed. K. Yamashita & T. Watanabe (Geneva: CERN), 411
- Kaastra, J. S., Raassen, A. J. J., de Plaa, J., & Gu, L. 2020, *SPEX X-ray spectral fitting package*, 3.07.00, Zenodo, doi:10.5281/zenodo.6948884
- Kaastra, J. S., Raassen, A. J. J., Mewe, R., et al. 2004, *A&A*, 428, 57
- Kallman, T., Bautista, M., Deprince, J., et al. 2021, *ApJ*, 908, 94
- King, A. L., Miller, J. M., & Raymond, J. 2012, *ApJ*, 746, 2
- Kraemer, S. B., Crenshaw, D. M., Gabel, J. R., et al. 2006, *ApJS*, 167, 161
- Krolik, J. H., & Kriss, G. A. 1995, *ApJ*, 447, 512
- Krolik, J. H., McKee, C. F., & Tarter, C. B. 1981, *ApJ*, 249, 422
- Krongold, Y., Jiménez-Bailón, E., Santos-Lleo, M., et al. 2009, *ApJ*, 690, 773
- Krongold, Y., Nicastro, F., Elvis, M., et al. 2007, *ApJ*, 659, 1022
- Laha, S., Guainazzi, M., Dewangan, G. C., Chakravorty, S., & Kembhavi, A. K. 2014, *MNRAS*, 441, 2613
- Laha, S., Reynolds, C. S., Reeves, J., et al. 2021, *NatAs*, 5, 13
- Mao, J., Kaastra, J. S., Mehdipour, M., et al. 2017, *A&A*, 607, A100
- Mauche, C. W., Liedahl, D. A., & Fournier, K. B. 2004, arXiv:astro-ph/0301633
- McKernan, B., Yaqoob, T., George, I. M., & Turner, T. J. 2003, *ApJ*, 593, 142
- McKernan, B., Yaqoob, T., & Reynolds, C. S. 2007, *MNRAS*, 379, 1359
- Mehdipour, M., Branduardi-Raymont, G., Kaastra, J. S., et al. 2011, *A&A*, 534, A39
- Mehdipour, M., Branduardi-Raymont, G., & Page, M. J. 2010, *A&A*, 514, A100
- Mehdipour, M., Kaastra, J. S., Costantini, E., et al. 2018, *A&A*, 615, A72
- Mehdipour, M., Kaastra, J. S., & Kallman, T. 2016, *A&A*, 596, A65
- Mehdipour, M., Kaastra, J. S., & Raassen, A. J. J. 2015, *A&A*, 579, A87
- Miller, J. M., Kaastra, J. S., Miller, M. C., et al. 2015, *Natur*, 526, 542
- Morales, R., Fabian, A. C., & Reynolds, C. S. 2000, *MNRAS*, 315, 149
- Nandra, K., Barret, D., Barcons, X., et al. 2013, arXiv:1306.2307
- Nandra, K., George, I. M., Mushotzky, R. F., Turner, T. J., & Yaqoob, T. 1997, *ApJ*, 476, 70
- Netzer, H. 1990, in *Active Galactic Nuclei: Saas-Fee Advanced Course 20. Lecture Notes 1990*. Swiss Society for Astrophysics and Astronomy XII, ed. R. D. Blandford (Berlin: Springer), 57
- Nicastro, F., Fiore, F., Perola, G. C., & Elvis, M. 1999, *ApJ*, 512, 184
- Peretz, U., Behar, E., Kriss, G. A., et al. 2018, *A&A*, 609, A35
- Piro, L., Ahlers, M., Coleiro, A., et al. 2022, *ExA*, 54, 23
- Ponti, G., Papadakis, I., Bianchi, S., et al. 2012, *A&A*, 542, A83
- Porquet, D., & Dubau, J. 2000, arXiv:astro-ph/9912065
- Porquet, D., Dubau, J., & Grosso, N. 2010, *SSRv*, 157, 103
- Reeves, J. N., Nandra, K., George, I. M., et al. 2004, *ApJ*, 602, 648
- Reynolds, C. S. 1996, PhD thesis, Univ. Cambridge
- Sadaula, D. R., Bautista, M. A., Garcia, J. A., & Kallman, T. R. 2022, arXiv:2205.04708
- Schwarz, J., McCray, R., & Stein, R. F. 1972, *ApJ*, 175, 673
- Silva, C. V., Uttley, P., & Costantini, E. 2016, *A&A*, 596, A79
- Smith, R. K., Abraham, M. H., Allured, R., et al. 2016, *Proc. SPIE*, 9905, 99054M
- Tarter, C. B., Tucker, W. H., & Salpeter, E. E. 1969, *ApJ*, 156, 943
- Tashiro, M., Maejima, H., Toda, K., et al. 2018, *Proc. SPIE*, 10699, 1069922
- Tombesi, F., Cappi, M., Reeves, J. N., et al. 2013, *MNRAS*, 430, 1102
- Tombesi, F., Meléndez, M., Veilleux, S., et al. 2015, *Natur*, 519, 436
- Veilleux, S., Meléndez, M., Sturm, E., et al. 2013, *ApJ*, 776, 27
- Wang, Y., Kaastra, J., Mehdipour, M., et al. 2022, *A&A*, 657, A77